Inorganic Chemistry
Article
pubs.acs.org/IC

Electronic Excited States of Tungsten(0) Arylisocyanides

Hana Kvapilová,[†,‡] Wesley Sattler,[§] Aaron Sattler,[§] Igor V. Sazanovich,[∥] Ian P. Clark,[∥] Michael Towrie,[∥] Harry B. Gray,[*,§] Stanislav Záliš,[*,†] and Antonín Vlček[*,†,⊥]

[†]J. Heyrovský Institute of Physical Chemistry, Czech Academy of Sciences, Dolejškova 3, CZ-182 23 Prague, Czech Republic

[‡]Department of Inorganic Chemistry, University of Chemistry and Technology, Prague, Technická 5, CZ-166 28 Prague, Czech Republic

[§]Beckman Institute, California Institute of Technology, Pasadena, California 91125, United States

[∥]Central Laser Facility, Research Complex at Harwell, STFC, Rutherford Appleton Laboratory, Harwell Oxford, Didcot, Oxfordshire OX11 0QX, United Kingdom

[⊥]Queen Mary University of London, School of Biological and Chemical Sciences, Mile End Road, London E1 4NS, United Kingdom

Supporting Information

ABSTRACT: $W(CNAryl)_6$ complexes containing 2,6-diisopropylphenyl isocyanide (CNdipp) are powerful photoreductants with strongly emissive long-lived excited states. These properties are enhanced upon appending another aryl ring, e.g., $W(CNdippPh^{OMe_2})_6$; $CNdippPh^{OMe_2}$ = 4-(3,5-dimethoxyphenyl)-2,6-diisopropylphenylisocyanide (Sattler et al. *J. Am. Chem. Soc.* **2015**, *137*, 1198−1205). Electronic transitions and low-lying excited states of these complexes were investigated by time-dependent density functional theory (TDDFT); the lowest triplet state was characterized by time-resolved infrared spectroscopy (TRIR) supported by density functional theory (DFT). The intense absorption band of $W(CNdipp)_6$ at 460 nm and that of $W(CNdippPh^{OMe_2})_6$ at 500 nm originate from transitions of mixed $\pi\pi^*$(C≡N−C)/MLCT(W → Aryl) character, whereby W is depopulated by ca. 0.4 e^- and the electron-density changes are predominantly localized along two equatorial molecular axes. The red shift and intensity rise on going from $W(CNdipp)_6$ to $W(CNdippPh^{OMe_2})_6$ are attributable to more extensive delocalization of the MLCT component. The complexes also exhibit absorptions in the 300−320 nm region, owing to W → C≡N MLCT transitions. Electronic absorptions in the spectrum of $W(CNXy)_6$ (Xy = 2,6-dimethylphenyl), a complex with orthogonal aryl orientation, have similar characteristics, although shifted to higher energies. The relaxed lowest $W(CNAryl)_6$ triplet state combines $\pi\pi^*$ excitation of a *trans* pair of C≡N−C moieties with MLCT (0.21 e^-) and ligand-to-ligand charge transfer (LLCT, 0.24−0.27 e^-) from the other four CNAryl ligands to the axial aryl and, less, to C≡N groups; the spin density is localized along a single Aryl−N≡C−W−C≡N−Aryl axis. Delocalization of excited electron density on outer aryl rings in $W(CNdippPh^{OMe_2})_6$ likely promotes photoinduced electron-transfer reactions to acceptor molecules. TRIR spectra show an intense broad bleach due to ν(C≡N), a prominent transient upshifted by 60−65 cm^{-1}, and a weak down-shifted feature due to antisymmetric C≡N stretch along the axis of high spin density. The TRIR spectral pattern remains unchanged on the femtosecond-nanosecond time scale, indicating that intersystem crossing and electron-density localization are ultrafast (<100 fs).

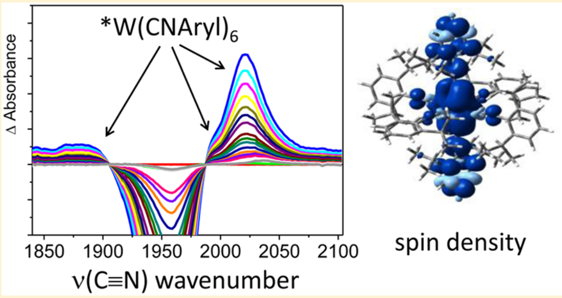

INTRODUCTION

In recent work on the photochemistry and photophysics of tungsten(0) hexakis arylisocyanide complexes, $W(CNAryl)_6$, we found that substituent variations dramatically affect their excited-state lifetimes, photostability, and emission quantum yields.[1,2] The introduction of *iso*-propyl groups at *ortho* positions of the aryl ring, which protects the tungsten from solvent interactions, greatly extends excited-state lifetimes over that of an analogous *ortho*-xylyl isocyanide complex, $W(CNXy)_6$ (Xy = 2,6-dimethylphenyl), which is less hindered around the central atom (Figure 1); notably, the coupling of another aryl group(s) to the 4-position of 2,6-diisopropylphenyl isocyanide (CNdipp) affords oligoarylisocyanide complexes, such as $W(CNdippPh^{OMe_2})_6$ ($CNdippPh^{OMe_2}$ = 4-(3,5-dimethoxyphenyl)-2,6-diisopropylphenylisocyanide), with excited-state lifetimes in the microsecond range, high (0.1−0.4) photoluminescence quantum yields, and very intense absorptions throughout the visible spectral region.[2] A fortuitous combination of these photophysical properties (Table 1) with reversible oxidations ($E°(W^+/W^0)) \approx -0.7$ V vs Fc^+/Fc in CH_2Cl_2) makes $W(CNAryl)_6$ complexes exceptionally strong photostable excited-state reductants ($E°(W^+/{*W^0})) \approx -2.8$ V vs. Fc^+/Fc or ca. − 2.2 vs. NHE), as demonstrated by phototriggered reduction of anthracene, benzophenone, acetophenone, and cobalticenium.[1,2] Dubbed[2] "bespoke photo-

Received: May 27, 2015
Published: August 12, 2015

DOI: 10.1021/acs.inorgchem.5b01203
Inorg. Chem. 2015, 54, 8518−8528

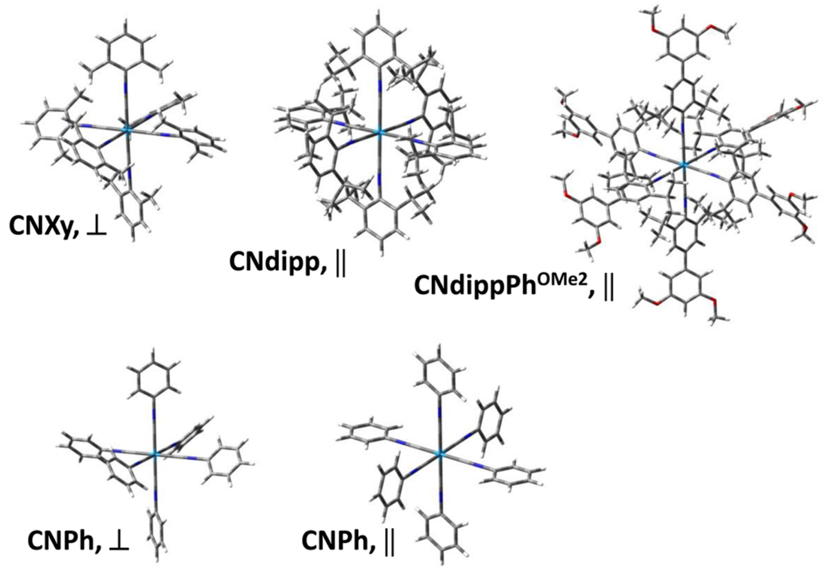

Figure 1. DFT-optimized structures. Top: predominant conformations of W(CNXy)$_6$, W(CNdipp)$_6$, and W(CNdippPh^{OMe_2})$_6$ in THF, denoted by the CNAryl ligand. Bottom: W(CNPh)$_6$ in orthogonal (⊥, T$_d$) and coplanar (||, C$_i$) conformations.

Table 1. Excited-State Properties of W(CNAr)$_6$ Complexes[a]

	emission (nm)	τ (ns)	ϕ_{PL}	k_r (s^{-1})	k_{nr} (s^{-1})	$E°(W^+/{*}W^0)$[b] V vs Fc$^+$/Fc
W(CNPh)$_6$/pyridine	638					
W(CNXy)$_6$/THF	580	17				
W(CNdipp)$_6$/THF	577	75	0.01	1.6×10^5	1.3×10^7	−3.00
W(CNdipp)$_6$/Tol	575	122	0.03	2.3×10^5	8.0×10^6	
W(CNdippPh^{OMe_2})$_6$/THF	627	1200	0.21	1.8×10^5	6.6×10^5	−2.79
W(CNdippPh^{OMe_2})$_6$/Tol	618	1650	0.42	2.6×10^5	3.5×10^5	

[a]Data from refs 1−3. τ: photoluminescence lifetime in degassed solutions; ϕ_{PL}: photoluminescence quantum yield; k_r and k_{nr}: radiative and nonradiative decay rate constants of the lowest excited state; $E°$: excited-state reduction potential. [b]In CH_2Cl_2/0.5 M Bu_4NPF_6.[2]

reductants", these compounds are promising photosensitizers, with potential applications in synthetic organic chemistry, light-energy conversion, and OLED technology.

Further developments of W(CNAryl)$_6$ photochemistry and photophysics, as well as photonic applications, depend critically on understanding the electronic nature of the intense visible absorptions and, importantly, of the lowest-lying emissive/reactive excited state. Interesting fundamental questions emerge about the (de)localization of excited electron density over the six ligands and, within each ligand, on the C≡N and aryl groups. To address these questions, we have employed time-dependent density functional theory (TDDFT) calculations to shed light on the electronic transitions, and we have elucidated the nature and dynamics of the lowest triplet state through density functional theory (DFT) calculations in combination with time-resolved spectroscopic experiments in the IR region of C≡N stretching vibrations.

■ EXPERIMENTAL SECTION

Materials. The isocyanide complexes were prepared and characterized as described previously.[1,2] Solutions for spectroscopic studies were prepared in Aldrich AtmosBag under argon, using anhydrous pentane and inhibitor-free tetrahydrofuran (Sigma-Aldrich) Sure/Seal packaged under nitrogen.

Time-Resolved IR Spectroscopy (TRIR). TRIR measurements in the ν(C≡N) spectral region were carried out using the ULTRA instrument at the STFC Rutherford Appleton Laboratory.[4] In the 0−3700 ps time domain, the sample solution was excited (pumped) at 400 nm, using frequency-doubled ~50 fs pulses of ~1 μJ energy at a 10 kHz repetition rate generated by titanium sapphire laser-based regenerative amplifier (Thales). Probe pulses obtained by difference-frequency generation cover about the 400 cm^{-1} range. Pump and probe beams were focused to an area of about 50 μm diameter. Time zero was set at the instant when coherent oscillations abate, measured with a 50 fs accuracy. In the nanosecond range, sample excitation was performed with 355 nm, ~0.7 ns fwhm, ~1 μJ laser pulses generated by an actively Q-switched AOT-YVO-20QSP/MOPA Nd:Vanadate diode-pumped microlaser that was electronically synchronized with the femtosecond probe system with less than 400 ps jitter.[5] The 400 or 355 nm pump beams were set at the magic angle to the probe. Pump and probe beams were focused to an area of about 100 and 70 μm diameter, respectively. Spectra at given time delays were recorded on two 128 element HgCdTe detectors (Infrared Associates) on a shot-by-shot basis with a 64 channel detector used for reference. Data were collected in pump-on/pump-off pairs to minimize the effect of long-term drift in the laser intensity. Sample solutions were placed in a 0.1 or 0.05 mm cell with 2 mm CaF_2 windows (Hellma) that was scanned-rastered across the irradiated area in two dimensions to prevent laser heating and decomposition of the sample. FTIR spectra were measured before and after TRIR experiments to check the sample stability. Spectral and kinetics fitting was performed using MicroCal Origin 9.0.

Computational Details. Electronic structures of W(CNAryl)$_6$ (Aryl = Ph, Xy, dipp and dippPh^{OMe_2}) complexes were calculated by density functional theory (DFT) methods using the Gaussian 09[6] program package. The Amsterdam Density Functional (ADF2014.01)[7,8] program was used for spin−orbit (SO) calculations. Molecular structures of W(CNdipp)$_6$, W(CNdippPh^{OMe_2}), and W(CNXy)$_6$ were optimized without any symmetry constraints. To assess the allowedness of electronic transitions, the structure of

W(CNPh)$_6$ has been optimized with the highest possible symmetry: T$_d$ and C$_i$ for orthogonal and coplanar conformations, respectively. (Calculating the latter within the idealized T$_h$ symmetry did not converge to a true minimum, producing imaginary vibrational frequencies.) G09/DFT calculations employed the Perdew, Burke, Ernzerhof (PBE0) hybrid functional.[9,10] The geometry of the lowest excited state was optimized by an unrestricted Kohn−Sham (UKS) approach, and all geometry optimizations were followed by vibrational analysis. Excitation energies were calculated by time-dependent DFT (TDDFT) at the optimized structures. For C, N, and O atoms, polarized double-ξ basis sets 6-31G(d)[11] were used, together with quasirelativistic effective core pseudopotentials and a corresponding optimized set of basis functions for W.[12,13] The solvent was described by the polarizable continuum model (PCM).[14] Within ADF, Slater-type orbital (STO) basis sets of a triple-ξ quality, with two polarization functions for the W atom and double-ξ with one polarization function for the remaining atoms, were employed. The basis set was represented by a frozen core approximation (1s for C, N, and O and 1s-4d for W were kept frozen). The PBE0 functional and the scalar relativistic (SR) zero order regular approximation (ZORA) were used. Solvent effect corrections were calculated using the COSMO model.[15] Spin−orbit excited states were calculated by a perturbative approach[16,17] from TDDFT-calculated spin-free excited states. IR and UV−vis spectra were simulated using Lorentzian (50 cm^{-1} fwhm) and Gaussian (3000 cm^{-1} fwhm) functions, respectively.

■ RESULTS

Molecular Structures. DFT calculations of all three complexes in THF and pentane solutions yield bonding parameters close to those previously determined crystallographically.[1,2,18] Each complex has a distorted octahedral structure in which the three Aryl−N≡C−W−C≡N−Aryl axes are nonequivalent (the three complexes differ in the mutual orientations of the aryl rings of *trans*-ligands, Figure 1). For W(CNdipp)$_6$ and W(CNdippPh$^{\mathrm{OMe_2}}$)$_6$, the *trans* aryls are nearly coplanar, 3−4° torsion angle, depending on the axis. These values are comparable to those determined crystallographically in the solid state: 3−7° and 3−12°, respectively. The calculated torsion angle between the two aromatic rings of W(CNdippPh$^{\mathrm{OMe_2}}$)$_6$ is 36−37° (crystallographic values are 37°, 37°, and 28° along the three axes[2]). In W(CNXy)$_6$, *trans* aryl rings along two axes are oriented nearly orthogonally (87°, 70°), while an intermediate orientation (56°) occurs along the third axis (82°, 76°, and 68° in the crystal structure[18]). Structures of the "opposite" conformations also were DFT-optimized: coplanar (1−7°) for W(CNXy)$_6$ and orthogonal (64−87°) for W(CNdipp)$_6$ and W(CNdippPh$^{\mathrm{OMe_2}}$)$_6$. The calculated free energy of orthogonal W(CNdipp)$_6$ in THF is 1614 cm^{-1} above that of the coplanar structure. The two conformations of W(CNXy)$_6$ have very similar free energies: the orthogonal conformation, which is present in the crystalline form,[18] was calculated in THF to be 466 cm^{-1} higher than the coplanar one. Calculated free energies are too similar to establish unequivocally the more stable structure. Conformational equilibria likely are present in solution for all three complexes (calculated structures of the complexes in both conformations are shown in Figure S1).

Electronic Structure and Absorption Spectra. Electronic absorption spectra of the investigated W(CNAryl)$_6$ complexes (Figure 2) show a UV band at 300−320 nm and a visible band around 460 nm that shifts to longer wavelengths with CNdippPh$^{\mathrm{OMe_2}}$ (~500 nm) and other oligoarylisocyanide ligands.[2] All complexes exhibit an additional near-UV band (a "middle band", 380−420 nm) whose relative intensity depends on the ligand: CNXy (380 nm, dominant) ≫ CNdipp (370 nm, weak) > CNdippPh$^{\mathrm{OMe_2}}$ (415 nm, very weak). In view of the structural difference between W(CNXy)$_6$ and W(CNdipp)$_6$, W(CNdippPh$^{\mathrm{OMe_2}}$)$_6$, the "middle band" is attributable to the orthogonal conformer, whereas the two bands at ~300 and 450−550 nm are characteristic of the coplanar structure, as both conformers are present in solution.

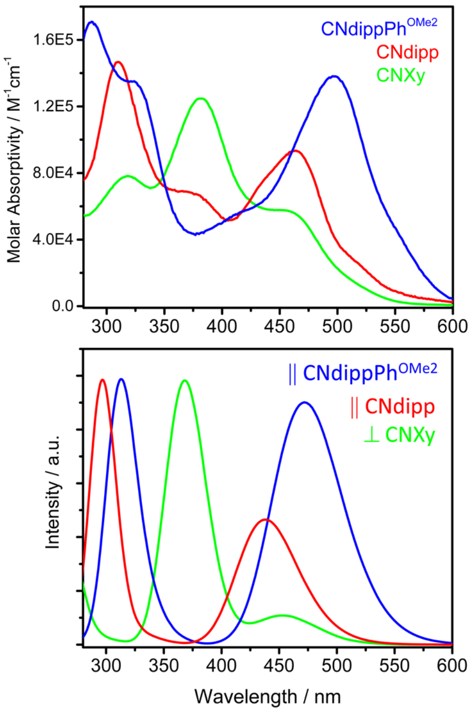

Figure 2. Top: experimental UV−vis absorption spectra of W(CNXy)$_6$ (green), W(CNdipp)$_6$ (red), and W(CNdippPh$^{\mathrm{OMe_2}}$)$_6$ (blue) in THF.[1,2] Bottom: TDDFT-simulated spectra of these complexes in their predominant conformations (PBE0, PCM-THF).

TDDFT-calculated absorption spectra of both conformers (Figure 3, top) indeed show that the "middle band" at ca. 380 nm (415 nm for CNdippPh$^{\mathrm{OMe_2}}$) belongs to the orthogonal conformer and the bands at 300−320 and 450−500 nm to the coplanar conformer. Calculations thus support the interpretation of the solution spectra as a superposition of absorptions due to the two conformers, orthogonal being predominant for W(CNXy)$_6$ and coplanar for W(CNdipp)$_6$ as well as W(CNdippPh$^{\mathrm{OMe_2}}$)$_6$. Comparison of experimental and calculated spectra of the three complexes (Figure 2) shows that TDDFT reproduces the spectra of the predominant conformation, including the red-shift and intensity rise on going from W(CNdipp)$_6$ to W(CNdippPh$^{\mathrm{OMe_2}}$)$_6$.

Calculated energies, compositions in terms of one-electron excitations, and pictures of relevant molecular orbitals are summarized for the most intense transitions of the three complexes in Tables S1−S5 and Figures S2−S6. Understanding the electronic transitions is helped by calculations of the phenylisocyanide complex W(CNPh)$_6$ that can be carried out using symmetry C$_i$ for coplanar and T$_d$ for orthogonal structures, respectively (see Supporting Information, pp. S40−S42). In summary, the W(CNAryl)$_6$ complexes have three close-lying HOMOs that are strongly W−C π bonding, each composed of ca. 50% metal dπ and ~35% of π*(C≡N) orbitals. Three closely spaced LUMOs of the coplanar structure are made up predominantly of π*(C≡N, Aryl) and π(N−Aryl) ligand orbitals, localized along one or two molecular axes

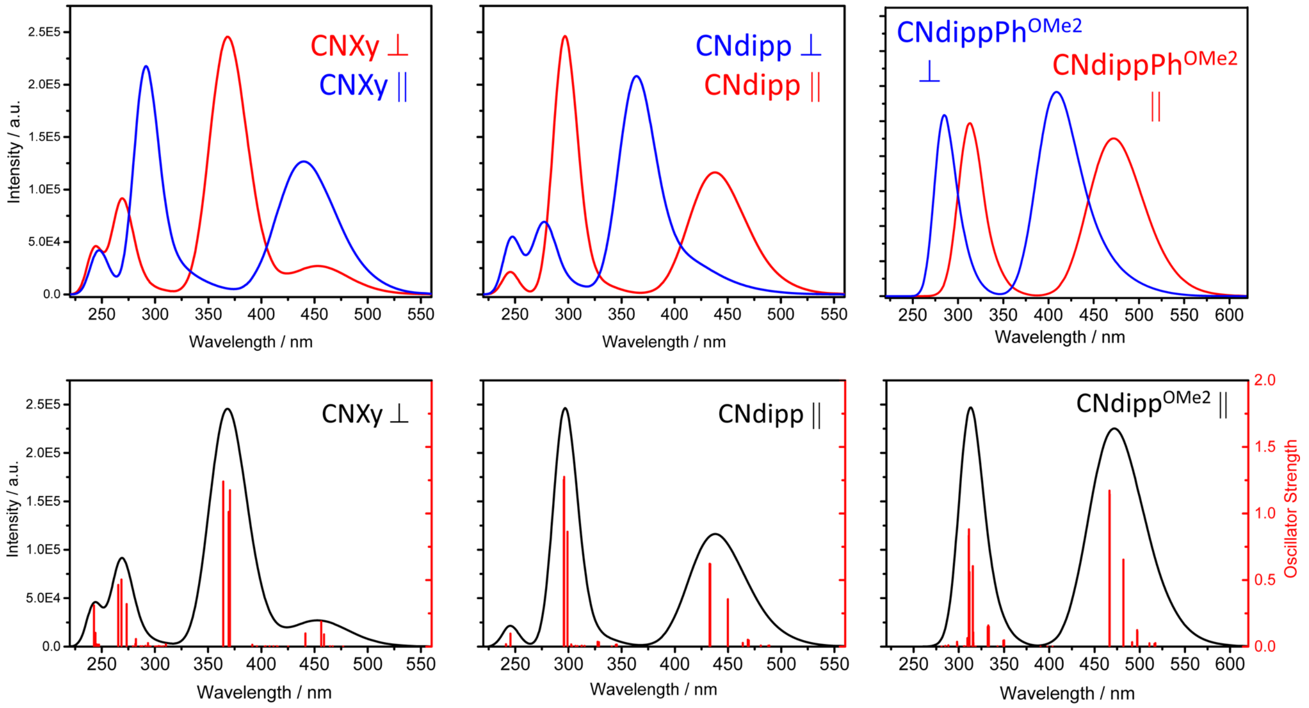

Figure 3. TDDFT-calculated spectra. Top: W(CNXy)$_6$, W(CNdipp)$_6$, and W(CNdippPh^{OMe_2})$_6$ in coplanar and orthogonal conformations. Spectra of predominant conformations are shown in red, the opposite ones in blue. The intensity scale of the W(CNdippPh^{OMe_2})$_6$ spectrum is 1.5× expanded. Bottom: Spectra of the three complexes together with calculated transitions. (The bars at 433 and 467 nm in the W(CNdipp)$_6$ and W(CNdippPh^{OMe_2})$_6$ spectra, respectively, correspond to two close-lying transitions.) (PBE0, PCM-THF)

(Figures S2−S6, Table S6). The equivalent set of orbitals in the orthogonal structure forms a LUMO+1 set occurring just above another set of three ligand-localized orbitals.

Various combinations of one-electron excitations from the HOMO set to the three LUMOs give rise to a dense manifold of singlet and triplet excited states (Figure 4, Tables S1−S5 and S7). The three allowed transitions responsible for the lowest intense absorption band are visualized by accompanying electron-density changes in Figures 5 and S2b, S3b, S4b, S5b, and S6b. The lowest strong band of the coplanar conformation and the main band of the orthogonal conformation are due to transitions that are largely delocalized along two (or one) molecular axes, respectively, having $\pi\pi^*$ character with respect to the corresponding pair(s) of *trans* Aryl−N≡C moieties, combined with charge transfer (MLCT) from the tungsten atom to the aryl rings that decreases the electron density at the metal atom by ~0.4 e$^-$. This general description is largely valid for all three complexes; however, in the case of W(CNdippPh^{OMe_2})$_6$, the MLCT component is partially delocalized over the second (-Ph^{OMe_2}) aryl ring (Figure 5, Table 2), where the electron density on the dipp and Ph^{OMe_2} rings increases by about 0.3 and 0.1 e$^-$, respectively. The 300−320 nm UV band of the coplanar conformation and the weaker far-UV band of the orthogonal species originate from predominantly W → π^*(C≡N) MLCT transitions along one or two axes, together with a minor contribution of ligand to ligand CT (LLCT) from another pair of CNAryl ligands (Figures S2b and 3b, bottom). These transitions are directed into a high-lying set of orbitals that are C≡N π-antibonding, lying in the aryl plane (e.g., LUMO+12,13,14 in W(CNdipp)$_6$, Figure S5a).

In terms of the nature and localization of the strong electronic transitions, there is little qualitative difference between the two conformations. The different appearance of the spectra (Figure 3) is caused by large blue-shifts of all the strongly allowed transitions on going from the coplanar to the orthogonal conformation (Figure 4), whereby the optically active π^*(C≡N, Aryl) LUMO as well as the horizontal π^*(C≡N) sets shift higher in energy, above other sets of ligand-localized orbitals. Detailed discussion based on the W(CNPh)$_6$ model is provided in Supporting Information, pp. S40−S42.

Experimental absorption spectra also show a shoulder on the long-wavelength side of the lowest strong band (500−550 nm (W(CNXy)$_6$, W(CNdipp)$_6$) and 550−600 nm for W(CNdippPh^{OMe_2})$_6$), followed by a weak red tail (Figure 2). To test possible contributions of spin-forbidden transitions to triplet states, we also have performed triplet TDDFT and perturbational spin−orbit TDDFT calculations of W(CNdipp)$_6$ in the coplanar conformation in THF. Low-lying triplet states are of similar nature and orbital parentage as the corresponding singlet excited states discussed above. Table S7 shows the lowest triplet states of W(CNdipp)$_6$ and eight other triplets lying in a 3115 cm^{-1} energy interval. They all originate from combinations of one-electron excitations between the HOMO and LUMO sets, although in different proportions than the singlets. Their possible contribution to the absorption spectrum was assessed by spin−orbit (SO) analysis performed on the W(CNdipp)$_6$ coplanar structure in idealized C_i symmetry. Simulated spectra calculated with and without SO coupling (Figure S8) are very similar, demonstrating that SO has a negligible effect. "Spin forbidden" transitions contribute only very little to the red tail, as they have no more than 6% singlet character (Table S8b). The strong transitions responsible for the two absorption bands have 94−99% singlet character. The low-energy shoulder and tail are therefore attributable to a series of weak transitions to low-lying, predominantly singlet

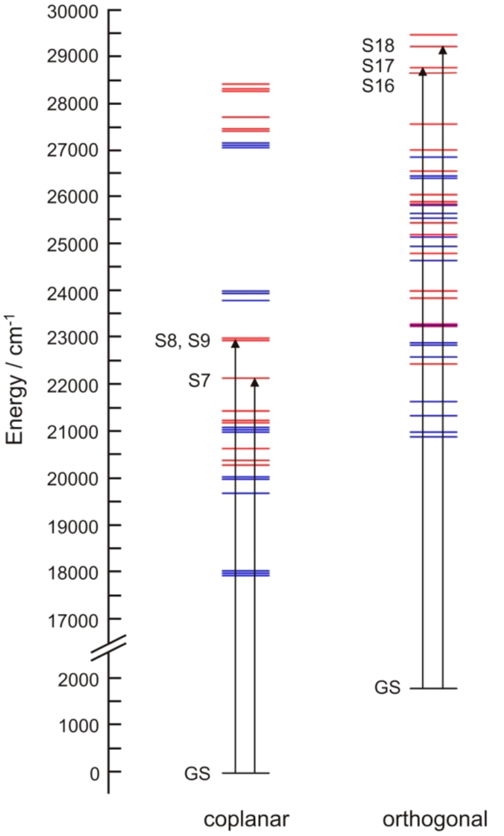

Figure 4. State diagram of W(CNdipp)$_6$ in coplanar and orthogonal conformations. Singlet and triplet states are shown by red and blue bars, respectively. Vertical arrows show the strong transitions responsible for the lowest intense absorption band (TDDFT, PBE0, PCM-THF).

states (Figure 4, red bars), whose nature is similar to that of the three strong transitions producing the lowest absorption band: $\pi\pi^*$(*trans*-C≡N−C)/MLCT(W → aryl) (Table S4). They are composed of various combinations of HOMO/HOMO−1/HOMO−2 → LUMO/LUMO+1/LUMO+2 one-electron excitations whose transition moments are relatively small, owing to poor orbital overlap.

Spectroscopic and Computational Characterization of the Lowest Excited State. Time-resolved infrared spectra were measured in the range of ν(C≡N) vibrations at selected time delays in femto−picosecond and nanosecond time domains following 400 and 355 nm excitation, respectively. Difference spectra are reported, where the positive and negative features correspond to photogenerated species (transients) and a depleted ground-state population (bleaches), respectively. Nanosecond TRIR spectra of W(CNdipp)$_6$ show a transient band at 2021 cm^{-1} that is blue-shifted by 63 cm^{-1} relative to the 1958 cm^{-1} bleach (Figure 6), with a shoulder at about 1995 cm^{-1}. The transient/bleach intensity ratio is about 0.25. Another, still weaker, broad transient band is apparent between 1870 and 1880 cm^{-1}. These features are superimposed on a broad background that extends across the IR spectral region. The transient and bleach bands decay with common single-exponential kinetics, without any changes in the spectral pattern or band positions. The ca. 60 ns TRIR lifetime is comparable to the emission lifetime[1,2] of 75 ns. The broad IR background absorption decays simultaneously with a lifetime of ca. 53 ns. Excited-state decay in THF leaves a long-lived weak feature at 2037 cm^{-1} that is apparent in the spectra after 200 ns; see the gray curves in Figure 6, measured at 500 and 1000 ns. This feature is due to a persistent photoproduct. It is virtually absent in pentane, where a much weaker persistent feature is apparent around 2006 cm^{-1}.

An intense bleach accompanied by (i) a weaker up-shifted transient band with a shoulder on its low-energy side, (ii) a weak down-shifted feature, and (iii) a broad background diminishing toward lower wavenumbers are the common TRIR features observed for all three isocyanide complexes (Figure 7). W(CNXy)$_6$ shows a very broad ground-state absorption attributable to conformational heterogeneity. Overlapping bleach and transient signals distort the W(CNXy)$_6$ spectrum and diminish the intensity of the ∼2014 cm^{-1} excited-state band, preventing an accurate determination of its position and relative intensity. Excited-state absorption of W(CNdippPh$^{\mathrm{OMe_2}}$)$_6$ is broader than in the case of W(CNdipp)$_6$ and it is shifted by about +65 cm^{-1} from the ground state, with a shoulder at ca. 2003 cm^{-1}. The single-exponential TRIR and luminescence[1,2] decay kinetics indicate that the excited state of each of the three complexes is present in a single conformation or that conformational exchange is much faster than the decay. The nanosecond TRIR transient signal is therefore attributed to the relaxed lowest triplet state in its predominant coplanar conformation as characterized by UKS-DFT optimization. (For W(CNXy)$_6$, another excited-state conformation in which Xy rings along only one axis are coplanar was calculated to have virtually identical free energy.) The broad weak background appears to be an inherent feature of the excited-state signal; it is attributable to a low-energy tail of a broad triplet−triplet electronic absorption band. The lowest electronic transition of this type was calculated at 1945 cm^{-1}, albeit very weak. (The first triplet−triplet transition allowed in the C$_i$ symmetry occurs at 7663 cm^{-1}.)

Whereas nanosecond TRIR spectra report on the thermally equilibrated lowest triplet state, spectra in the femto−picosecond range provide information on relaxation processes,[19,20] including intersystem crossing.[21] TRIR transient features of W(CNdipp)$_6$ appear as early as 50 fs after excitation and do not undergo any dynamic shifts (Figure 8). The peak intensity of the up-shifted excited-state band at ∼2020 cm^{-1} grows with a 6 ps lifetime. The background absorbance partially decays throughout the whole spectral range with a ∼ 5 ps lifetime (measured at several wavenumbers between 1844 and 1880 cm^{-1}). Temporal evolution of TRIR spectra was complete at about 20 ps. The observed intensity changes are attributable to vibrational cooling of the excited molecule and its first solvent shell and, possibly, also to a conformational change. (Ring rotation after exciting the orthogonal conformation is expected to occur very fast, with no or a very low barrier.) The picosecond background decay is attributable to cooling of low-frequency vibrations and/or relaxation-induced blue shift of the corresponding triplet−triplet electronic transition. The absence of any changes in the spectral pattern and band positions indicates that the observed femto−picosecond spectral features belong to the same excited state (the lowest triplet) and conformation as observed in the nanosecond spectra. Population of the lowest triplet by electronic and structural relaxation of the optically populated singlet state (including intersystem crossing) occurs within the instrument time resolution, faster than 200 fs.

In the case of W(CNdippPh$^{\mathrm{OMe_2}}$)$_6$, the rise of the excited-state IR band is accompanied by a dynamical shift to higher

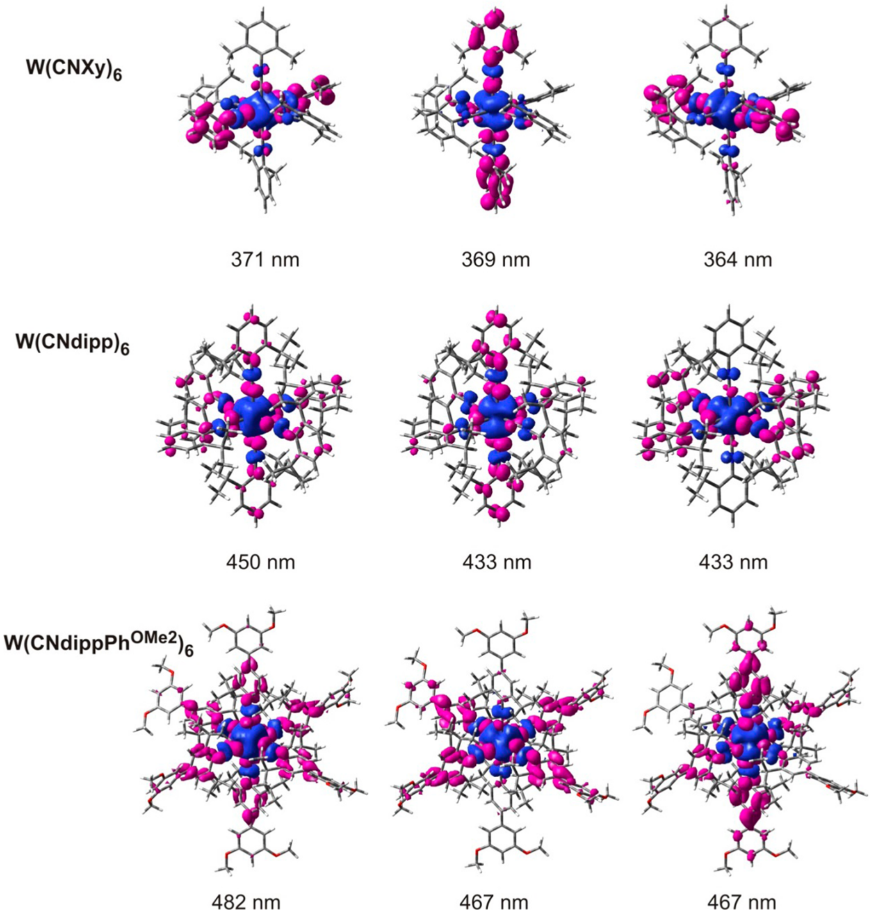

Figure 5. Electron-density changes accompanying the three allowed transitions responsible for the lowest intense absorption band of the more stable conformation of each complex. Calculated transition wavelengths are specified (compare Figure 3). Purple and blue colors indicate increasing and diminishing electron density, respectively (TDDFT, PBE0, PCM-THF).

wavenumbers from about 2007 cm^{-1} at 50 fs to 2020 cm^{-1} at 1 ns (Figure 8, inset) that takes place without any change in the overall spectral pattern (Figure S10). It appears that relaxation of the lowest triplet excited state of $W(CNdippPh^{OMe_2})_6$ and its environment involves some electron-density redistribution. This behavior could be caused by specific solvation that also is evidenced by a solvent effect on excited-state lifetimes (Table 1).[2] The results of ultrafast TRIR dynamics of $W(CNXy)_6$, which are not presented herein, reveal complicated behavior, owing to partial photodecomposition and, very likely, to conformational changes.

The ground-state IR band of the $W(CNAryl)_6$ complexes consists of three closely spaced vibrations that result from splitting of the octahedral T_{1u} stretching mode, $\nu(C{\equiv}N)$. DFT analysis (Table S9) shows that each of these three vibrations is composed of a predominant antisymmetric C≡N stretch and small aromatic ring deformation of a *trans* pair of isocyanide ligands, combined with minor contributions from antisymmetric vibrations of the other two ligand pairs (Figures 9 and S11). Further three in-phase and out-of-phase symmetrical $\nu(C{\equiv}N)$ vibrations were calculated at higher energies and possess very low IR intensities (Table S9). The low-wavenumber shoulder observed in the $W(CNXy)_6$ spectrum (Figure 7, bottom) likely belongs either to a minor conformation or to a combination mode that is beyond the harmonic approximation of the DFT vibrational analysis. DFT-calculated IR spectra of the lowest triplet state match the experimental TRIR spectra (Figures 6, S9, and S12–S14), validating the UKS optimization of the lowest-triplet structure and calculated electron (spin) density distribution that will be presented below. The three IR active $\nu(C{\equiv}N)$ modes essentially retain their basic nature upon excitation (Figures 9 and S11) but undergo large shifts: one of them to lower and the other two to higher energies. The calculated energy splitting of the two up-shifted vibrations depends on the CNAryl ligand, 22, 3, and 32 cm^{-1} for CNXy, CNdipp, and $CNdippPh^{OMe_2}$, respectively, explaining the larger width of the $W(CNdippPh^{OMe_2})_6$ transient band as compared to $W(CNdipp)_6$ (Figure 7). The calculated shift between the mean ground state and highest excited state $\nu(C{\equiv}N)$ wavenumbers (63 and 65 cm^{-1} for $W(CNdipp)_6$ and $W(CNdippPh^{OMe_2})_6$, respectively) also matches experimental values.

The calculated spin density distribution in the relaxed lowest triplet state is distinctly axial, as demonstrated in Figure 10 for $W(CNdippPh^{OMe_2})_6$ and Figure S15 for $W(CNXy)_6$ and $W(CNdipp)_6$. The spin density has π-symmetry with respect to a single *trans* Aryl−N≡C−W−C≡N−Aryl moiety. It is the $\nu(C{\equiv}N)$ vibration along this axis that is shifted downward upon excitation, indicating that the bonding acquires some W=C=N=Aryl character, in agreement with the calculated C≡N bond lengthening (by 0.005−0.008 Å), N−C(Aryl) contraction (−0.04 Å), and W−C elongation (+0.02 Å). Inspection of changes of Mulliken charges on the relevant molecular fragments (Table 2) reveals that the lowest triplet combines

Table 2. Differences of Mulliken Charges on Molecular Fragments of the W(CNAryl)$_6$ Complexes upon the Three Lowest Strong Vertical Singlet Transitions (Tables S3−S5) and between the Lowest Triplet State and the Ground State in Their Optimized Geometries (PBE0/PCM-THF)

W(CNXy)$_6$, orthogonal

	optimized lowest triplet	TDDFT singlet 16 371 nm	TDDFT singlet 17 369 nm	TDDFT singlet 18 364 nm
W	0.179	0.399	0.415	0.430
1 CN	−0.126	−0.009	−0.040	0.037
2 CN	0.034	0.061	0.082	−0.022
3 CN	0.043	−0.040	−0.003	0.058
1 Xy	−0.317	0.026	−0.449	−0.056
2 Xy	0.098	0.002	−0.026	−0.452
3 Xy	0.089	−0.440	0.021	0.005

W(CNdipp)$_6$, coplanar

	optimized lowest triplet	TDDFT singlet 7 450 nm	TDDFT singlet 8 433 nm	TDDFT singlet 9 433 nm
W	0.207	0.442	0.440	0.441
1 CN	−0.126	−0.041	−0.026	−0.032
2 CN	0.021	−0.028	0.025	−0.068
3 CN	0.045	−0.026	−0.070	0.028
1 ^{i}PrPh	−0.319	−0.125	−0.090	−0.165
2 ^{i}PrPh	0.074	−0.112	−0.060	−0.183
3 ^{i}PrPh	0.098	−0.111	−0.219	−0.022

W(CNdippPh^{OMe_2})$_6$, coplanar

	optimized lowest triplet	TDDFT singlet 7 482 nm	TDDFT singlet 8 467 nm	TDDFT singlet 9 467 nm
W	0.214	0.437	0.434	0.434
1 CN	−0.095	−0.017	−0.044	0.042
2 CN	0.022	0.011	0.044	−0.040
3 CN	0.043	−0.010	0.010	0.007
1 ^{i}PrPh	−0.263	−0.119	−0.183	−0.045
2 ^{i}PrPh	0.068	−0.088	−0.016	−0.207
3 ^{i}PrPh	0.089	−0.111	−0.130	−0.078
1 Ph^{OMe_2}	−0.126	−0.038	−0.062	−0.016
2 Ph^{OMe_2}	0.021	−0.029	−0.009	−0.066
3 Ph^{OMe_2}	0.026	−0.036	−0.041	−0.031

$\pi\pi^*$ excitation of a *trans* pair of C$\equiv$N−C(Aryl) moieties with MLCT and ligand-to-ligand CT components (LLCT), whereby the electron density (0.4−0.5 e$^-$ in total) is transferred from the tungsten atom (MLCT, 0.21 e$^-$) and the four equatorial CNAryl ligands (LLCT, 0.24−0.27 e$^-$) to the aryl rings (72% for CNXy and CNdipp; 80% for CNdippPh^{OMe_2}) and CN groups (30−20%) of the two axial ligands. Vibrations of the C$\equiv$N bonds of the electron-depopulated equatorial ligands are shifted to higher wavenumbers, giving rise to the main transient TRIR band. Excited electron density is delocalized along two *trans* C$\equiv$N bonds as well as the aryl ring(s). In the case of W(CNdippPh^{OMe_2})$_6$, the electron density on the dipp and terminal −Ph(OMe)$_2$ groups increases by 0.26 and 0.13 e$^-$, that is 0.39 e$^-$ in total, which is slightly higher than the 0.32 e$^-$ increase on the two axial dipp rings in W(CNdipp)$_6$ (Table 2). Figure 10 also shows spin density localized along the inter-ring C−C π bond that results in changing the torsion angle from 36° to 28° and a small bond contraction (−0.01 Å) upon excitation.

Finally, we consider spin−orbit effects on the lowest triplet excited state and the possibility of thermal population of other close-lying electronic states. An SO-TDDFT calculation of W(CNdipp)$_6$ was performed at the geometry of the lowest triplet using idealized C_i symmetry (Table S10). The calculated zero-field splitting of the lowest triplet to three A_u SO components is rather small, 13 cm^{-1}. The singlet content, which varies from 0% (the lowest SO state) to 2%, involves admixture of low-lying $\pi\pi^*$(*trans* Aryl−N$\equiv$C)/MLCT(W → Aryl) singlet states discussed above. The next two SO states (both A_u) occur 1663 and 1684 cm^{-1} higher in energy, followed by a dense manifold of A_u SO states. The lowest A_g SO state was calculated 6425 cm^{-1} above the lowest triplet. It follows that, at room temperature, the lowest triplet system (i.e., the set of lowest three SO states) is populated almost exclusively (99.95%), in accord with the above assignment of the TRIR spectrum.

■ DISCUSSION

In the ground state, each W(CNAryl)$_6$ complex has a distorted pseudooctahedral structure. The orientation of the *trans* aryl rings depends on the substituent: orthogonal for CNXy and coplanar for CNdipp, CNdippPh^{OMe_2}, and other oligo-arylisocyanides.[2] Nevertheless, the "opposite" conformation also is present as a minor form in solution. Their ground-state electronic structures feature three delocalized W−C π-bonding HOMOs that are composed mainly of W 5dπ and π^*(C$\equiv$N) fragment orbitals and three π^*(C$\equiv$N)/π(N−C(Aryl))/π^*-(Aryl) LUMOs (Figures S2a, S3a, S4a, S5a, and S6a, Table S6).

Electronic absorption spectra and excited-state properties of W(CNAryl)$_6$ complexes are hard to predict. In principle, spectroscopic features attributable to MLCT to C$\equiv$N or to aryl groups, as well as $\pi\pi^*$ intraligand transitions, are all likely. Of course, conjugation between π^*(C$\equiv$N) and aryl π orbitals must be taken into account.[22,23] Localization of excited electron

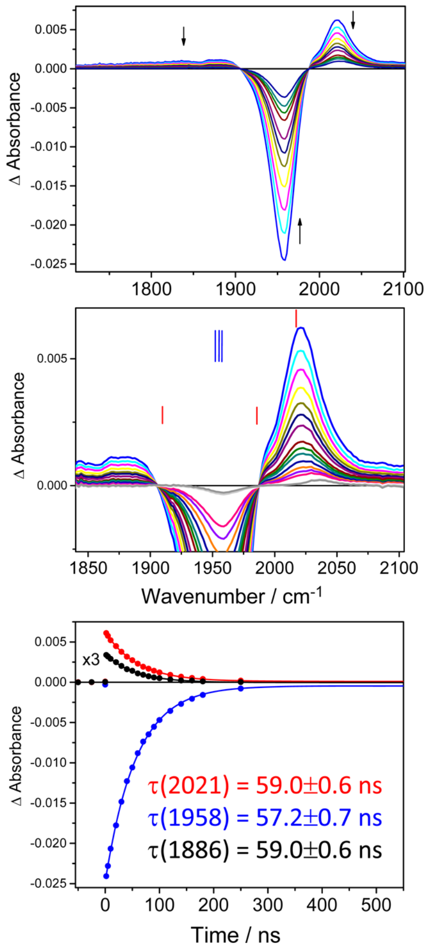

Figure 6. Nanosecond TRIR spectra of W(CNdipp)$_6$ in THF measured at selected time delays in the 2−1000 ns range after 0.8 ns, 355 nm laser-pulse excitation. Top: full-range spectra evolving in the direction of the arrows. Middle: detail of the transient bands, blue and red bars show DFT-calculated ground- and excited-state wavenumbers, respectively (Table S9). Bottom: kinetics profiles measured at specified wavenumbers. (Very similar spectra were obtained in pentane (Figure S9).)

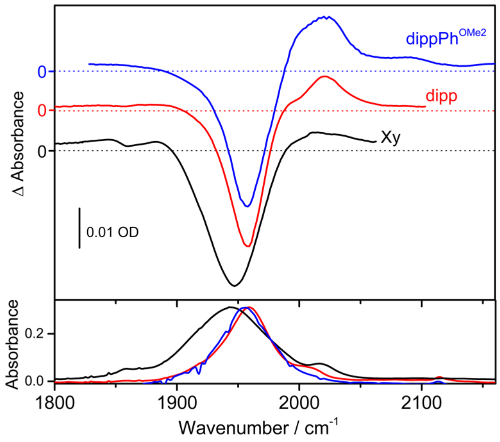

Figure 7. TRIR spectra of the three isocyanide complexes in THF: W(CNXy)$_6$ (black, excited at 400 nm, measured after 1.5 ns), W(CNdipp)$_6$ (red, 355 nm, 2 ns), and W(CNdippPhOMe2)$_6$ (blue, 400 nm, 1.5 ns). The spectra are vertically offset by 10 mOD. The 2 ns spectrum of W(CNdipp)$_6$ is independent of the excitation wavelength. Ground-state FTIR spectra are shown in the lower panel.

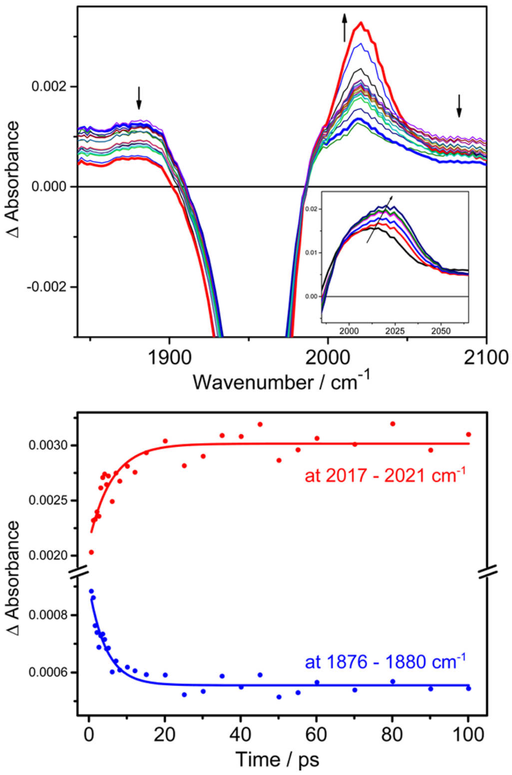

Figure 8. Femto−picosecond TRIR spectra of W(CNdipp)$_6$ and W(CNdippPh^{OMe_2})$_6$ measured in THF after 400 nm, 50 fs excitation. Top: TRIR of W(CNdipp)$_6$ measured every 50 fs from 0 to 650 fs (50 fs shown in blue-bold), at 1.15 ps (black, third from the top at 2020 cm^{-1}), 10 ps (blue, second from the top), and 80 ps (red-bold). Inset: Spectra of W(CNdippPh^{OMe_2})$_6$ in the transient region measured at 0.7, 5, 10, 45, 100, and 1000 ps in the direction of the arrow. (W(CNdippPh^{OMe_2})$_6$ spectra in a broader wavenumber range are shown in Figure S10.) Bottom: Time evolution of the maximum transient (red) and background (blue) signal intensities of W(CNdipp)$_6$. The curves show the corresponding single-exponential fits. (Very similar behavior was observed in pentane.)

density over all or a limited set of CNAryl ligands is another open question. On the basis of analogy with carbonyl complexes of heavy metals (W(0), Re(I)),[24−28] ligand-field (d-d) transitions, which are expected to be highly delocalized due to strong covalency, would occur at very high energies. Our TDDFT calculations have shown that the strong visible absorptions originate from transitions into singlet states that combine intraligand $\pi\pi^*$ excitation of *trans* C≡N−C(Aryl) moieties and W → Aryl MLCT, decreasing the electron density on W by about 0.4 e$^-$. These transitions are localized along two equatorial axes in the coplanar complexes W(CNdipp)$_6$ and W(CNdippPh^{OMe_2})$_6$, whereas localization along a single axis is found for W(CNXy)$_6$ (Figure 5). In the case of W(CNdippPh^{OMe_2})$_6$, the MLCT contribution involves both the proximal (dipp) and distal (Ph(OMe)$_2$) rings. More extensive conjugation and MLCT occurring over a larger spatial region explain the pronounced red-shift and intensity rise on going from W(CNdipp)$_6$ to W(CNdippPh^{OMe_2})$_6$ and other oligoarylisocyanide complexes.[2] The UV absorption bands at ca. 300 and 250 nm for coplanar and orthogonal conformations, respectively, are attributable to W → CN MLCT transitions localized along one or two axes. Electron density is excited into π^*(C≡N) orbitals that lie in the aryl plane. LLCT from the other pair(s) of CNAryl ligands also contributes (Figures S2b

DOI: 10.1021/acs.inorgchem.5b01203
Inorg. Chem. 2015, 54, 8518−8528

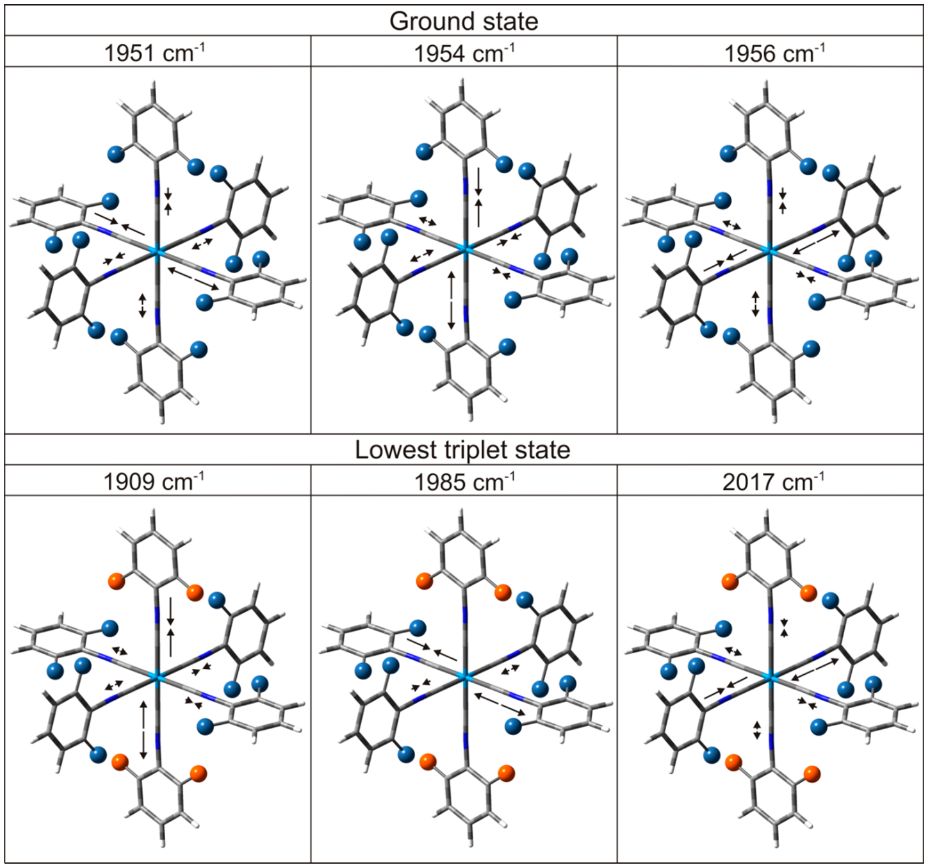

Figure 9. Ground-state (top) and excited-state (bottom) IR-active vibrations of W(CNdipp)$_6$. ^{i}Pr substituents are shown as spheres. The orange color denotes the dippNC-W-CNdipp moiety with the highest excited-state spin-density localization (compare Figure 10). Vibrations of W(CNXy)$_6$ and W(CNdippPh^{OMe_2})$_6$ are analogous, Figure S11.

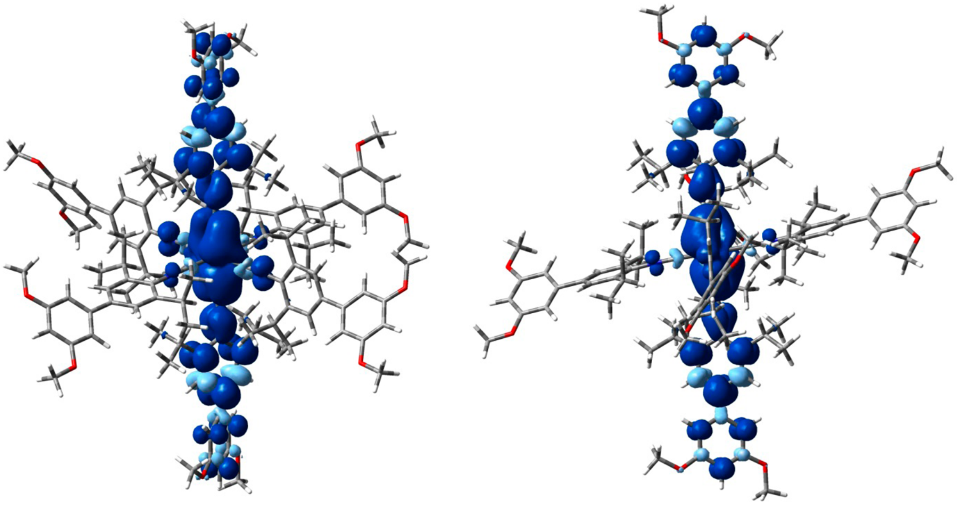

Figure 10. Spin density distribution in the lowest triplet state of W(CNdippPh^{OMe_2})$_6$ shown in two molecular orientations. DFT-UKS, PBE0/PCM-THF.

and S3b). No LF-type transitions were calculated below 7 eV (∼180 nm).

From photochemical and photophysical points of view, singlet excited states of W(CNAryl)$_6$ complexes are important, as they function as efficient light-energy gateways into the molecule, but they are too short-lived (<100 fs) to be involved in photochemical reactions. Indeed, only the lowest triplet state was detected by fs-TRIR spectra, indicating that electronic relaxation is ultrafast, taking place in a few tens of femtoseconds, much like in metal polypyridines.[29−31] Intersystem crossing (ISC) in W(CNAryl)$_6$ likely follows multiple pathways within the dense manifold of low-lying singlet and triplet states (Figure 4) that are of similar character but differ in the particular combinations of depopulated HOMO orbitals (Tables S4 and S7) and, hence, in spatial orientation. This situation opens nonradiative singlet−triplet SO channels among excited states, whereby the spin-momentum change is compensated by orbital rotation, which is a prerequisite for ultrafast ISC.[21,32]

Interestingly, the relaxed lowest triplet state (T1) is largely localized along one molecular axis, and with $\pi\pi^*$(C≡N−C), LLCT, and MLCT contributions, the charge transfer is directed to a pair of *trans* aryl rings and, less, CN groups (Table 2, Figures 10 and S15). The electron density transferred from the four equatorial ligands, which is slightly larger (0.24 e^- for $W(CNdipp)_6$) than that from the tungsten atom (0.21 e^-, Table 2), originates from equatorial aryl (0.17 e^-) as well as CN (0.07 e^-) groups. This asymmetry between the axial and equatorial CNAryl ligands is clearly manifested in the TRIR spectral pattern, whereby two antisymmetric ν(C≡N) vibrations of the depopulated ligands shift to higher energies relative to the ground state, giving rise to the transient band and a shoulder on its low-wavenumber side, while the antisymmetric ν(C≡N) vibration along the axis of highest spin-density localization shifts downward (compare Figures 9, 10, and S11−S15). The spectroscopic manifestation is complicated by overlap of excited-state bands with the broad and intense ground-state bleach that largely obscures the down-shifted band, which appears only as a weak feature around 1880 cm^{-1} and partly merges with the background. The TRIR transient signal is thus dominated by upshifted vibrations and the +63 cm^{-1} shift from the ground-state position qualitatively reflects depopulation of π^*(C≡N) orbitals of equatorial CNAryl ligands, owing to diminishing π back-donation and an overall electron-density decrease through MLCT and LLCT components of the T1 state, respectively. Still, the 2020 cm^{-1} excited-state ν(C≡N) vibration occurs lower than that in the oxidized complex, $[W(CNdipp)_6]^+$ (2040 cm^{-1}).[3]

This peculiar charge distribution and the axial symmetry of T1 are observed only for the structurally relaxed state: Singlet excited states (Table 2, Figure 5) as well as the lowest vertical triplet (Table S11, Figure S16) are predominantly localized equatorially along two axes, and the LLCT component is very small (negligible for $CNdippPh^{OMe_2}$). The axial spin-density localization and charge redistribution due to an increased LLCT contribution apparently take place in the course of electronic and structural relaxation of the optically populated state, within our instrument time resolution (<200 fs). Part of the T1 relaxation together with solvation then contributes to the IR intensity rise (and band shift in the case of $W(CNdippPh^{OMe_2})_6$) during the first ~20 ps.

High phosphorescence quantum yields[2] (Table 1) contrast with the small calculated T1 zero-field splitting (13 cm^{-1}) and singlet admixture (1−2%) in the two higher SO sublevels (Table S10b). SO coupling in T1 is rather weak for an excited state of a heavy-metal complex with partial MLCT character, possibly owing to the axial spin-density distribution. The strong phosphorescence is not caused by large radiative rate constants ($1{-}2 \times 10^5$ s^{-1})[2] but, instead, by slow nonradiative decay that also extends the excited-state lifetime to tens of nanoseconds ($W(CNdipp)_6$) or microseconds ($W(CNdippPh^{OMe_2})_6$ and other oligoarylisocyanides).[2] Slow nonradiative decay is attributable to the large delocalization of excited electron density over a pair of *trans* ligands that, for oligoarylisocyanides, extends over the outer rings. Extensive delocalization minimizes excited-state distortions and, hence, the Franck−Condon factor of nonradiative decay to the ground state.[33,34] $W(CNdipp)_6$-type complexes are relatively photochemically inert as the W−C bonds are not weakened in the excited state and the *ortho* ^{i}Pr groups disfavor associative interactions with the tungsten atom, leaving outer-sphere excited-state electron (or energy) transfer as a major photochemical pathway.[1−3] However, small polar solvent molecules interact with excited complexes, as manifested by solvent-dependent emission lifetimes[2] and a low-yield photoreaction observed in THF but not in pentane.

Ultrafast population of the T1 state and axial distribution of excited electron density over *trans* aryl rings are very relevant to photoredox reactivity. Bimolecular electron transfer will be facilitated by interactions between electron-rich aromatic groups of the excited complex with oxidants and, at the same time, limited by orientational requirements. Synthetic chemistry permitting, structural variations are expected to tune excited-state redox properties. Bulky substituents on outer rings and increasing the length of the oligoaryl ligand would diminish bimolecular interactions. (Indeed, photoreduction of benzophenone and, especially, acetophenone by $W(CNdippPh^{OMe_2})_6$ is slower than by $W(CNdipp)_6$.[2]) Appending electron-accepting groups at the 4-position of aryl rings (preferentially only on a single pair of *trans* ligands) would shift absorption deeper in the visible spectral region and decrease somewhat the T1 excited-state energy, making it a thermodynamically weaker reductant, but it would enhance electronic interactions with redox partners, possibly increasing electron-transfer rates. Such groups also could facilitate attachment of the $W(CNAryl)_6$ units to *n*-semiconductors, for employment as photosensitizers in solar fuels devices. Incorporation into molecular wires and conducting polymers would be a promising approach for polymeric solar cells or OLED-type applications. We can also imagine making electron-transfer dyads (or triads) with electron acceptors (or an acceptor and a donor) attached to aryl rings, whereby excitation of the $W(CNAryl)_6$ core would lead to long-lived charge-separated states. Our present understanding of the T1 excited-state structure requires the $W(CNAryl)_6$ unit to be linked to other redox components along a single molecular axis of supramolecular constructs.

■ ASSOCIATED CONTENT

Ⓢ Supporting Information

The Supporting Information is available free of charge on the ACS Publications website at DOI: 10.1021/acs.inorgchem.5b01203.

Figures of DFT-optimized solution structures, detailed tables, and figures showing calculated intense electronic transitions (orbital compositions, shapes and localizations of relevant MOs, transition energies, and electronic density differences), triplet and spin−orbit excited states, calculated ν(C≡N) vibrations and comparison of calculated and experimental IR and TRIR spectra, spin-density distribution of optimized lowest triplet state, spin−orbit states at the T1 geometry, electron-density differences, and Mulliken charge changes in the vertical lowest triplet states (PDF)

■ AUTHOR INFORMATION

Corresponding Authors

*E-mail: zalis@jh-inst.cas.cz.
*E-mail: hbgray@caltech.edu.
*E-mail: a.vlcek@qmul.ac.uk.

Notes

The authors declare no competing financial interest.

■ ACKNOWLEDGMENTS

This work was supported by the STFC Rutherford Appleton Laboratory, Ministry of Education of the Czech Republic Grant LH13015 (program KONTAKT II), COST Action CM1202. Research at Caltech was supported by the NSF CCI Solar Fuels Program (CHE-1305124) and the Arnold and Mabel Beckman Foundation.

■ REFERENCES

(1) Sattler, W.; Ener, M. E.; Blakemore, J. D.; Rachford, A. A.; LaBeaume, P. J.; Thackeray, J. W.; Cameron, J. F.; Winkler, J. R.; Gray, H. B. *J. Am. Chem. Soc.* **2013**, *135*, 10614−10617.

(2) Sattler, W.; Henling, L. M.; Winkler, J. R.; Gray, H. B. *J. Am. Chem. Soc.* **2015**, *137*, 1198−1205.

(3) Mann, K. R.; Gray, H. B.; Hammond, G. S. *J. Am. Chem. Soc.* **1977**, *99*, 306−307.

(4) Greetham, G.; Burgos, P.; Cao, Q.; Clark, I. P.; Codd, P.; Farrow, R.; George, M. W.; Kogimtzis, M.; Matousek, P.; Parker, A. W.; Pollard, M.; Robinson, D.; Xin, Z.-J.; Towrie, M. *Appl. Spectrosc.* **2010**, *64*, 1311−1319.

(5) Towrie, M.; Parker, A. W.; Vlček, A., Jr.; Gabrielsson, A.; Blanco Rodriguez, A. M. *Appl. Spectrosc.* **2005**, *59*, 467−473.

(6) Frisch, M. J.; Trucks, G. W.; Schlegel, H. B.; Scuseria, G. E.; Robb, M. A.; Cheeseman, J. R.; Scalmani, G.; Barone, V.; Mennucci, B.; Petersson, G. A.; Nakatsuji, H.; Caricato, M.; Li, X.; Hratchian, H. P.; Izmaylov, A. F.; Bloino, J.; Zheng, G.; Sonnenberg, J. L.; Hada, M.; Ehara, M.; Toyota, K.; Fukuda, R.; Hasegawa, J.; Ishida, M.; Nakajima, T.; Honda, Y.; Kitao, O.; Nakai, H.; Vreven, T.; Montgomery, J. A., Jr.; Peralta, J. E.; Ogliaro, F.; Bearpark, M.; Heyd, J. J.; Brothers, E.; Kudin, K. N.; Staroverov, V. N.; Kobayashi, R.; Normand, J.; Raghavachari, K.; Rendell, A.; Burant, J. C.; Iyengar, S. S.; Tomasi, J.; Cossi, M.; Rega, N.; Millam, J. M.; Klene, M.; Knox, J. E.; Cross, J. B.; Bakken, V.; Adamo, C.; Jaramillo, J.; Gomperts, R.; Stratmann, R. E.; Yazyev, O.; Austin, A. J.; Cammi, R.; Pomelli, C.; Ochterski, J. W.; Martin, R. L.; Morokuma, K.; Zakrzewski, V. G.; Voth, G. A.; Salvador, P.; Dannenberg, J. J.; Dapprich, S.; Daniels, A. D.; Farkas, O.; Foresman, J. B.; Ortiz, J. V.; Cioslowski, J.; Fox, D. J.; *Gaussian 09*; Revision C.01, Gaussian, Inc.: Wallingford CT, 2009.

(7) Te Velde, G.; Bickelhaupt, F. M.; van Gisbergen, S. J. A.; Fonseca Guerra, C.; Baerends, E. J.; Snijders, J. G.; Ziegler, T. *J. Comput. Chem.* **2001**, *22*, 931−967.

(8) *ADF2014.02, SCM, Theoretical Chemistry*; Vrije Universiteit: Amsterdam, The Netherlands; http://www.scm.com.

(9) Perdew, J. P.; Burke, K.; Ernzerhof, M. *Phys. Rev. Lett.* **1996**, *77*, 3865−3868.

(10) Adamo, C.; Barone, V. *J. Chem. Phys.* **1999**, *110*, 6158−6170.

(11) Krishnan, R.; Binkley, J. S.; Seeger, R.; Pople, J. A. *J. Chem. Phys.* **1980**, *72*, 650−654.

(12) Andrae, D.; Häussermann, U.; Dolg, M.; Stoll, H.; Preuss, H. *Theor. Chim. Acta* **1990**, *77*, 123−141.

(13) Martin, J. M. L.; Sundermann, A. *J. Chem. Phys.* **2001**, *114*, 3408.

(14) Cossi, M.; Rega, N.; Scalmani, G.; Barone, V. *J. Comput. Chem.* **2003**, *24*, 669−681.

(15) Klamt, A.; Schüürmann, G. *J. Chem. Soc., Perkin Trans. 2* **1993**, 799−805.

(16) Wang, F.; Ziegler, T. *J. Chem. Phys.* **2005**, *123*, 154102.

(17) Wang, F.; Ziegler, T.; van Lenthe, E.; van Gisbergen, S.; Baerends, E. J. *J. Chem. Phys.* **2005**, *122*, 204103.

(18) Lockwood, M. A.; Fanwick, P. E.; Rothwell, I. P. *Organometallics* **1997**, *16*, 3574−3575.

(19) Liard, D. J.; Busby, M.; Matousek, P.; Towrie, M.; Vlček, A., Jr. *J. Phys. Chem. A* **2004**, *108*, 2363−2369.

(20) Blanco-Rodríguez, A. M.; Busby, M.; Ronayne, K. L.; Towrie, M.; Grădinaru, C.; Sudhamsu, J.; Sýkora, J.; Hof, M.; Záliš, S.; Di Bilio, A. J.; Crane, B. R.; Gray, H. B.; Vlček, J. A. *J. Am. Chem. Soc.* **2009**, *131*, 11788−11800.

(21) Blanco-Rodríguez, A. M.; Kvapilová, H.; Sýkora, J.; Towrie, M.; Nervi, C.; Volpi, G.; Záliš, S.; Vlček, A., Jr. *J. Am. Chem. Soc.* **2014**, *136*, 5963−5973.

(22) Mann, K. R.; Cimolino, M.; Geoffroy, G. L.; Hammond, G. S.; Orio, A. A.; Albertin, G.; Gray, H. B. *Inorg. Chim. Acta* **1976**, *16*, 97−101.

(23) Bursten, B. E.; Fenske, R. F. *Inorg. Chem.* **1977**, *16*, 963−964.

(24) Záliš, S.; Farrell, I. R.; Vlček, A., Jr. *J. Am. Chem. Soc.* **2003**, *125*, 4580−4592.

(25) Záliš, S.; Busby, M.; Kotrba, T.; Matousek, P.; Towrie, M.; Vlček, A., Jr. *Inorg. Chem.* **2004**, *43*, 1723−1734.

(26) Záliš, S.; Milne, C. J.; El Nahhas, A.; Blanco-Rodriguez, A. M.; van der Veen, R. M.; Vlček, A., Jr. *Inorg. Chem.* **2013**, *52*, 5775−5785.

(27) Rosa, A.; Baerends, E. J.; van Gisbergen, S. J. A.; van Lenthe, E.; Groeneveld, J. A.; Snijders, J. G. *J. Am. Chem. Soc.* **1999**, *121*, 10356−10365.

(28) Vlček, A., Jr.; Záliš, S. *Coord. Chem. Rev.* **2007**, *251*, 258−287.

(29) Cannizzo, A.; van Mourik, F.; Gawelda, W.; Zgrablic, G.; Bressler, C.; Chergui, M. *Angew. Chem., Int. Ed.* **2006**, *45*, 3174−3176.

(30) Bräm, O.; Messina, F.; Baranoff, E.; Cannizzo, A.; Nazeeruddin, M. K.; Chergui, M. *J. Phys. Chem. C* **2013**, *117*, 15958−15966.

(31) Bräm, O.; Messina, F.; El-Zohry, A. M.; Cannizzo, A.; Chergui, M. *Chem. Phys.* **2012**, *393*, 51−57.

(32) Cannizzo, A.; Blanco-Rodríguez, A. M.; Nahhas, A.; Šebera, J.; Záliš, S.; Vlček, A., Jr.; Chergui, M. *J. Am. Chem. Soc.* **2008**, *130*, 8967−8974.

(33) Treadway, J. A.; Loeb, B.; Lopez, R.; Anderson, P. A.; Keene, F. R.; Meyer, T. J. *Inorg. Chem.* **1996**, *35*, 2242−2246.

(34) Strouse, G. F.; Schoonover, J. R.; Duesing, R.; Boyde, S.; Jones, W. E.; Meyer, T. J. *Inorg. Chem.* **1995**, *34*, 473−487.